Vacuum 195 (2022) 110690

Contents lists available at ScienceDirect

Vacuum

journal homepage: www.elsevier.com/locate/vacuum

Short communication

Indentation strain rate sensitivity of laser-powder bed fused and electron beam melted Ti–6Al–4V

Harish Chandra Kaushik [a], Shawkat Imam Shakil [b], Babak Shalchi Amirkhiz [c,d], Mohsen Mohammadi [d], Ebrahim Asadi [a], Meysam Haghshenas [b], Amir Hadadzadeh [a,*]

[a] Department of Mechanical Engineering, University of Memphis, Memphis, TN, USA
[b] Department of Mechanical, Industrial and Manufacturing Engineering, University of Toledo, Toledo, OH, USA
[c] CanmetMATERIALS, Natural Resources Canada, Hamilton, ON, Canada
[d] Marine Additive Manufacturing Centre of Excellence (MAMCE), University of New Brunswick, Fredericton, NB, Canada

ARTICLE INFO

Keywords:
Indentation strain rate sensitivity
Additive manufacturing
L-PBF
EBM
Ti–6Al–4V

ABSTRACT

Indentation hardness (H_{in}) and strain rate sensitivity (SRS) of additive manufactured Ti–6Al–4V (Ti64) alloys fabricated through both laser powder bed fusion (L-PBF) and electron beam melting (EBM) are investigated. One major difference between these processes is the higher cooling rates associated with the L-PBF. The indentation tests were performed at loading rates of 1, 10, and 50 mN/s. The L-PBF alloy showed a higher hardness value (3.45 GPa at 1 mN/s, 3.57 GPa at 10 mN/s, and 3.66 GPa at 50 mN/s) being correlated with its finer grain structure as compared with the EBM counter material (3.12 GPa at 1 mN/s, 3.37 GPa at 10 mN/s, and 3.55 GPa at 50 mN/s). The indentation SRS was explained based on the print orientation and dislocation density. EBM-Ti64 shows a higher SRS (0.0335 compared with 0.0147 in the L-PBF alloy) due to the rotation of α-prismatic planes along the building direction.

1. Introduction

Ti–6Al–4V (Ti64), an α+β alloy, shares the maximum of total titanium production due to its exceptional properties [1]. These include high fracture toughness and ductility, good weldability, superior fatigue, and corrosion behaviors, lightweight characteristic, and biocompatibility making Ti64 a high caliber candidate for the aerospace and biomedical industries [2,3]. Additive manufacturing (AM) technologies facilitate the fabrication of complex near-net-shaped components directly from a powder or wire feedstock [4]. Therefore, it is necessary to develop processing-microstructure-properties relationships of AM-Ti64 to ensure the fabrication of components with desired properties [5]. To fabricate AM components from metal powder, laser-powder bed fusion (L-PBF) and electron beam melting (EBM) are the most promising techniques [6]. One significant difference between the two processes is the solidification or cooling rates associated with these two methods [7]. Such a difference results in the formation of different microstructures, as L-PBF-Ti64 exhibits fine acicular α' martensite, while EBM-Ti64 possesses fine needle-like α Widmanstatten microstructure [8,9] These microstructures result in significant variation in the mechanical properties of Ti64 processed by L-PBF and EBM [10]. Literature manifests the comparative studies between mechanical properties of L-PBF and EBM Ti64, including tensile and fatigue properties [11]. The present work focuses on the micromechanical properties and an investigation of the relationship between microstructure and indentation strain rate sensitivity (SRS: m_{ind}) using electron backscatter diffraction (EBSD) and nanoindentation with a constant load but varying strain rate. The depth-sensing indentation technique is a unique testing method to evaluate the local mechanical properties using a small volume of the material. Moreover, various properties (e.g., fracture toughness, activation volume, activation energy, plasticity and wear resistance, etc.) can be quantified and assessed using indentation technique.

2. Experimental procedure

EBM and L-PBF processes were employed to fabricate cylindrical samples with dimensions of 120 mm × 9.5 mm (length × diameter) in the horizontal orientation. ARCAM EBM Q10 system (located in Woburn, MA) with maximum power 3000W and powder particles size of 45–100 μm was used to print EBM samples. For L-PBF samples, an EOS

* Corresponding author.
E-mail address: amir.hadadzadeh@memphis.edu (A. Hadadzadeh).

https://doi.org/10.1016/j.vacuum.2021.110690
Received 9 August 2021; Received in revised form 8 September 2021; Accepted 18 October 2021
Available online 19 October 2021

M-290 with respective values of 400W and 20–60 μm, available at the University of Memphis (Metal Additive Manufacturing Laboratory) was used. The iMicro Nanoindenter (KLA instruments) was employed to perform depth-sensing indentation tests. The instrument was equipped with an InForce 1000 head and a diamond Berkovich indenter (tip radius = 100 nm). The microstructural analysis was conducted using a field emission gun scanning electron microscope equipped with an EBSD. The EBSD studies were conducted along the building direction (z), with details reported in Ref. [12].

3. Microstructure and texture

Fig. 1 (a) shows the grain size distribution of L-PBF and EBM-Ti64 alloys, obtained from the EBSD results. The L-PBF process resulted in the evolution of α′ laths with a smaller width (thickness) compared to α laths developed in the EBM-Ti64, nearly by an order of magnitude. This is due to higher cooling rates present in the L-PBF process. In fact, the typical cooling rates in the L-PBF and EBM processes are ~10^6 K/s and ~10^4 K/s, respectively [13]. As a result, the microstructure of L-PBF-Ti64 is much finer than its EBM counterpart. Figures 1 (b) and (c) show the L-PBF and EBM-Ti64 EBSD inverse pole figures (EBSD-IPF). A significant difference in the grain size and morphology is observed between the two samples. While a basketweave needle-type α′ grain structure was developed in the L-PBF-Ti64, the EBM-Ti64 consists of a Widmanstatten α structure. In addition to the size and morphological dissimilarities, another difference between the α′ and α phases is the lattice distortion in the former as a result of rapid cooling in the L-PBF process [14]. Nevertheless, both α′ and α phases possess an HCP crystal structure. The EBSD pole figures (PF) reveal partial rotation of α grains and alignment of α-prismatic planes along the building direction in the EBM-Ti64 alloy [15]. This could be due to the lower solidification rate during the EBM process and longer available time for the evolution of the preferred texture. On the other hand, the L-PBF-Ti64 possesses a more random texture, due to the evolution of various variants of α' martensite in the prior β grains [16].

4. Micromechanical properties

Fig. 2 shows the indentation load-depth and indentation hardness-depth plots of L-PBF and EBM Ti64 samples. The load-depth (*P-h*) graph in Fig. 2 (a and b) shows that, for a constant load of 200 mN, the indentation depth is greater in the EBM sample, under different loading rates. Such behavior indicates that the L-PBF-Ti64 sample has a higher strength due to its higher hardness [17]. Microstructural differences of L-PBF-Ti64 and EBM-Ti64 validate the higher strength of L-PBF-Ti64 as this material possesses a finer microstructure compared to the EBM-Ti64 as shown in Fig. 1(a). Such a finer lath width enhances the strength through the Hall-Petch mechanism [18]. Fig. 2(c and d), indentation

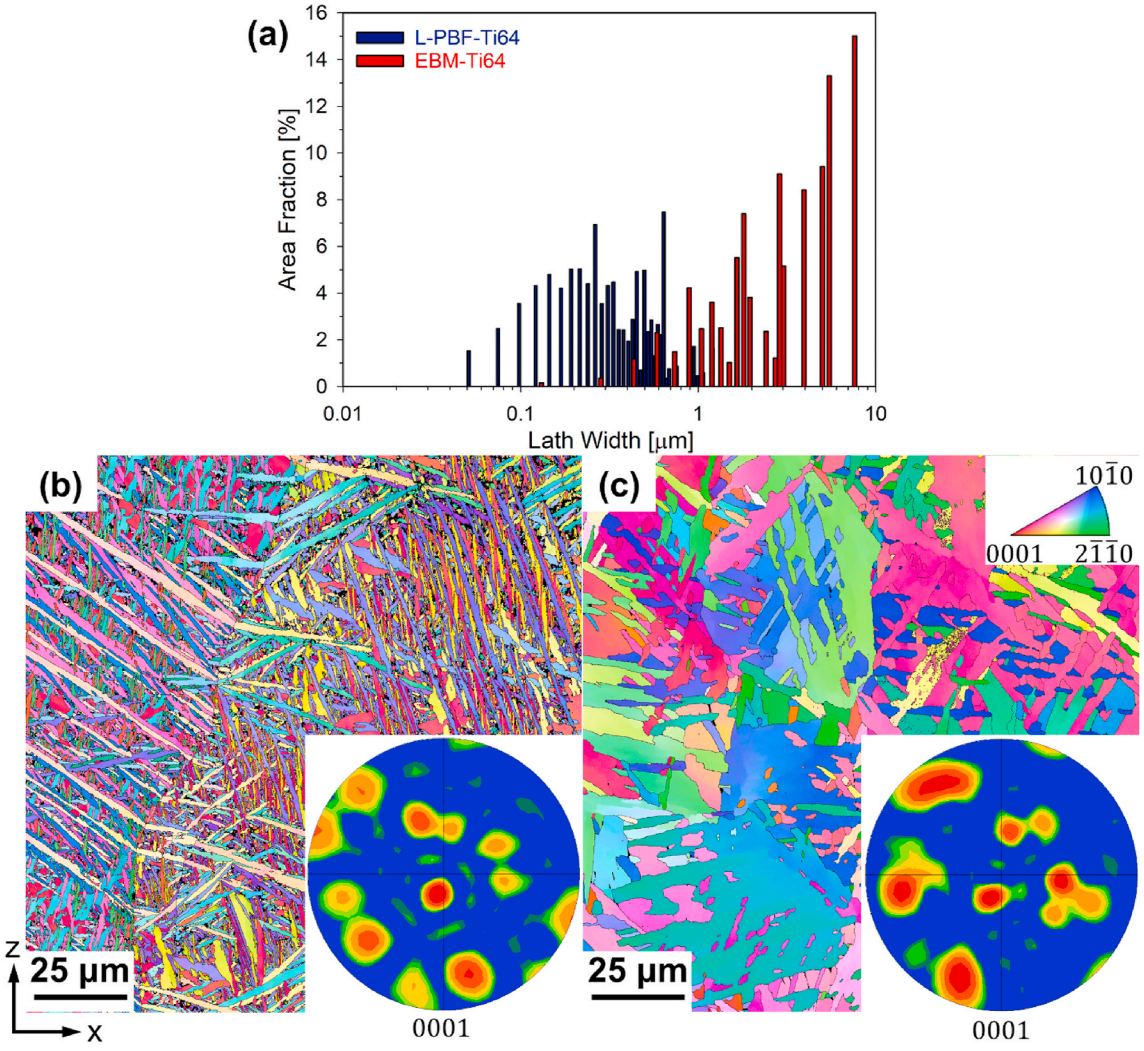

Fig. 1. (a) Grain size distribution of L-PBF and EBM Ti64, EBSD IPF-Z images of (b) L-PBF and (c) EBM Ti64. The inserts on the IPF maps show the (0001) pole figures [9].

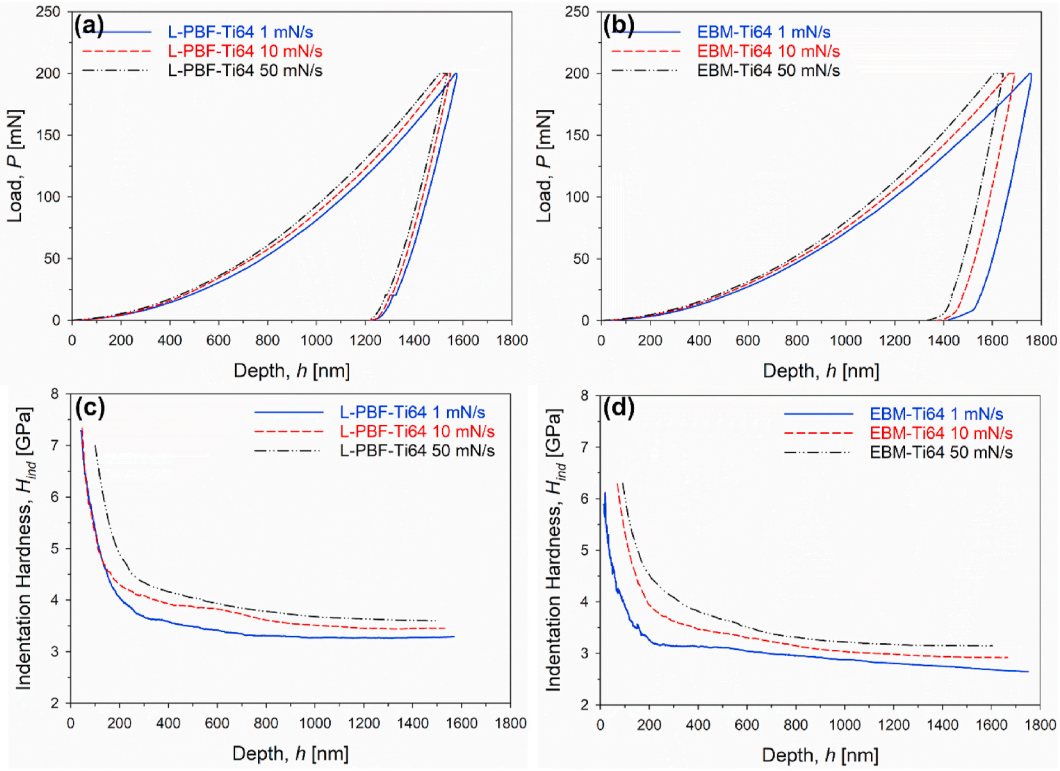

Fig. 2. Representative load-depth curves for (a) L-PBF-Ti64 and (b) EBM-Ti64, indentation size effect (ISE) for (c) L-PBF-Ti64, and (d) EBM-Ti64.

hardness versus depth, shows higher hardness for lower indentation depth, a typical indentation size effect (ISE). For an indentation depth beyond 200 nm, in the current study, the indentation hardness becomes independent of depth due to a balance between work hardening and dynamic recovery of dislocations. ISE can be seen both in the microscale as well as nanoscale. Reasons associated with ISE in microscale are strain gradient hardening and geometrically necessary dislocations (GNDs) and in the nanoscale are dislocation starvation [19,20]. The observed ISE is attributed to strain gradient plasticity, due to the presence of GNDs near the surface, and dislocation-starved plasticity (DSP), due to the absence of dislocation at the early stages of indentation [21]. GNDs are the dislocations required to accommodate the micro-plastic deformation. The nucleation of GNDs associated with the pop-in behavior is noticed during nano-indentation. In a broad sense, nano-indentation testing has three regimes: the elastic regime, the regime in which the hardness is dominated by GNDs also known as the elastic-plastic transition point, and finally the macroscopic regime dominated by statistically stored dislocations (SSDs). For the initiation of pop-in or nucleation of GNDs, the shear stress or load underneath the indenter should reach a critical value that depends upon the strength of the material. The estimated critical load, which is fundamentally the maximum load that a material can deform elastically is given by Ref. [22]:

$$F_{crit} = \left(\frac{G}{2\pi}\frac{1}{0.12}\right)^3 \frac{R^2}{E^2} \tag{1}$$

where G is shear modulus, R is the radius of displaced sphere and E is the elastic modulus of the material.

GNDs do not make a significant contribution to plastic deformation but they impede the motion of SSDs, which results in work hardening [23]. GNDs density (ρ_G) can be calculated as [24]:

$$\rho_G = \frac{4\gamma}{bD} \tag{2}$$

where γ is the average shear strain, b is the magnitude of Burger's vector, and D is indent diameter (diagonal of the indent), which is proportional to indentation depth. It should be noted that, this equation (and the next one) are valid for a Berkovich indenter. Hardness in the context of dislocation density is represented as [24]:

$$H \approx Gb\left[\rho_S + \frac{4\gamma}{bD}\right]^{1/2} \tag{3}$$

where ρ_S is statistically stored density. It is clear from Eq. (2) that GNDs density decreased with indentation depth so as hardness from Eq. (3).

The relationship between indentation hardness and grain size for polycrystalline materials has been discussed by modified strain gradient theory [25]. As reported, the relationship predicts for the same indentation depth, a specimen with a finer microstructure gives higher hardness; a typical Hall-Petch effect. In other words, L-PBF with smaller lath width shows higher resistance to plastic deformation resulting in a smaller indent size or indentation diameter (D), and gives a higher hardness value according to Eq. (3).

For the same maximum load of 200 mN, the displacement is higher for a smaller load rate and at the same time, different hardness values were observed at a different depth, which confirms that both L-PBF and EBM-Ti64 alloys are rate-sensitive though for the EBM sample the SRS is more pronounced. SRS depends on slip transfer across the grain boundary, grain orientation classified as hard and soft grains, grain size, and dislocation density [26–30].

5. Strain rate sensitivity

Fig. 3 shows the hardness versus strain rate for the L-PBF-Ti64 and EBM-Ti64 samples. The value of SRS for both samples was evaluated using the information presented in Fig. 3, as $m_{ind} = \frac{d(\ln H_{ind})}{d(\ln \dot{\varepsilon}_{ind})}$ [27]. As seen, EBM-Ti64 possesses a higher m_{ind} value than the L-PBF-Ti64.

SRS in dual-phase (α/β) titanium alloys is highly affected by slip transfer across the phase boundaries [26]. A high density of dislocation pile-ups has been observed at the α/β interface for dual-phase Ti-alloy, a

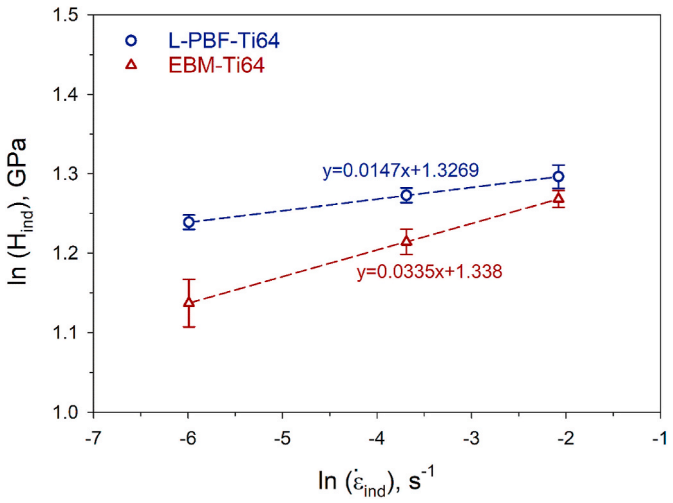

Fig. 3. SRS comparison for L-PBF-Ti64 and EBM-Ti64.

reason why both β volume fraction and β morphology has a significant effect [26]. These dislocations can transmit easily across boundaries having similar burger vectors, known as direct transmission. Other than this, the Frank-Read source at the front of the dislocation pile-up leads to the nucleation of dislocations and indirect transmission. Based on the strain hardening and dislocation plasticity (ease of dislocation transmission) the grains are classified as soft or hard grains [27]. The literature [28] shows a noticeable difference between α-basal, α-prismatic, and β-phase SRS and properties associated with it, like activation energy and activation volume. It has been observed that prismatic slip activity manifests 2–3 times elevated values of SRS compared to basal as it has more slip localization and a higher hardening gradient [28]. Referring to the EBSD-IPF and PF results of the samples, the HCP crystals in the EBM-Ti64 have rotated towards the building direction. As a result, more prismatic planes are parallel to the building direction in the EBM-Ti64, which were hit by the indenter during the nanoindentation experiments. Consequently, a higher SRS was evaluated for the EBM-Ti64 alloy.

Other than grain orientation, grain size, and dislocation density also affect the SRS. Literature confirms a lower value of SRS for ultra-fine grains of BCC metals compare to coarse grains, but the opposite trend was seen for the FCC metals [29]. Due to the paucity of experimental results, the relationship between grain size and SRS is unestablished for HCP materials in ultra-fine and coarse grain regimes [31] and the available results do not show any specific trend for SRS of HCP metals [32]. Nevertheless, in the current study, the material with a finer grain structure (i.e. L-PBF-Ti64) possesses a lower SRS. Eq. (4) represents the relationship between SRS and dislocation density which shows higher dislocation density leads to lower SRS [30]:

$$SRS = \frac{B}{s f_a \rho b^2} \tag{4}$$

where B is damping factor, s is Schmidt factor, f_a is constant (2/3 according to Ref. [30]), and ρ is dislocation density. It has been reported that the dislocation density of L-PBF-Ti64 is higher than EBM-Ti64 by the order of two [33,34], which results in a lower SRS of L-PBF, well correlated with our results.

6. Summary

The micromechanical properties of L-PBF-Ti64 and EBM-Ti64 alloys were studied using the depth-sensing indentation testing technique. The L-PBF-Ti64 exhibits a higher hardness due to its finer microstructure, comprised of needle-shaped martensite α' phase. The EBM-Ti64 microstructure consisted of α phase with a comparatively lower hardness value. Both alloys revealed a typical ISE. The SRS comparison of L-PBF-Ti64 and EBM-Ti64 showed a higher SRS value for the EBM-Ti64 (i.e., ~0.034 versus 0.015). The alignment of α-prismatic planes along the building direction is the main reason for a higher SRS in the EBM-Ti64 as α-prismatic has a higher hardening gradient. Other than orientation, dislocation density has an inverse effect on SRS. Characteristically, the dislocation density in the L-PBF-Ti64 is higher than that in the EBM-Ti64; therefore, a lower SRS was detected in the L-PBF-Ti64 alloys.

Data availability statement

The raw/processed data required to reproduce these findings cannot be shared at this time as the data also forms part of an ongoing study.

Declaration of competing interest

The authors declare that they have no known competing financial interests or personal relationships that could have appeared to influence the work reported in this paper.

Acknowledgment

Funding provided from various agencies including NSERC and NBIF is acknowledged.

References

[1] D. Vasudevan, P. Balashanmugam, Study of thermal behaviour on titanium alloys (Ti-6Al-4V), J. Eng. Sci. Technol. 12 (2017) 2064–2077.
[2] R.R. Boyer, An overview on the use of titanium in the aerospace industry, Mater. Sci. Eng. 213 (1996) 103–114, https://doi.org/10.1016/0921-5093(96)10233-1.
[3] Q. Yan, B. Chen, N. Kang, X. Lin, S. Lv, K. Kondoh, S. Li, J.S. Li, Comparison study on microstructure and mechanical properties of Ti-6Al-4V alloys fabricated by powder-based selective-laser-melting and sintering methods, Mater. Char. 164 (2020), https://doi.org/10.1016/j.matchar.2020.110358.
[4] M. Attaran, The rise of 3-D printing: the advantages of additive manufacturing over traditional manufacturing, Bus. Horiz. 60 (2017) 677–688, https://doi.org/10.1016/j.bushor.2017.05.011.
[5] J. Mezzetta, J.P. Choi, J. Milligan, J. Danovitch, N. Chekir, A. Bois-Brochu, Y. F. Zhao, M. Brochu, Microstructure-properties relationships of Ti-6Al-4V parts fabricated by selective laser melting, Int. J. Precis. Eng. Manuf. - Green Technol. 5 (2018) 605–612, https://doi.org/10.1007/s40684-018-0062-1.
[6] D. Dev Singh, T. Mahender, A. Raji Reddy, Powder bed fusion process: a brief review, Mater. Today Proc. (2020) 2–7, https://doi.org/10.1016/j.matpr.2020.08.415.
[7] P.K. Gokuldoss, S. Kolla, J. Eckert, Additive manufacturing processes: selective laser melting, electron beam melting and binder jetting-selection guidelines, Materials 10 (2017), https://doi.org/10.3390/ma10060672.
[8] B. Wysocki, P. Maj, R. Sitek, J. Buhagiar, K.J. Kurzydłowski, W. Świeszkowski, Laser and electron beam additive manufacturing methods of fabricating titanium bone implants, Appl. Sci. 7 (2017) 1–20, https://doi.org/10.3390/app7070657.
[9] A. Hadadzadeh, E. Asadi, S. Imam Shakil, B. Shalchi Amirkhiz, M. Mohammadi, M. Haghshenas, Indentation-derived mechanical properties of Ti-6Al-4V: laser-powder bed fusion versus electron beam melting, Mater. Lett. 301 (2021) 130273, https://doi.org/10.1016/j.matlet.2021.130273.
[10] X. Zhao, S. Li, M. Zhang, Y. Liu, T.B. Sercombe, S. Wang, Y. Hao, R. Yang, L. E. Murr, Comparison of the microstructures and mechanical properties of Ti-6Al-4V fabricated by selective laser melting and electron beam melting, Mater. Des. 95 (2016) 21–31, https://doi.org/10.1016/j.matdes.2015.12.135.
[11] H.K. Rafi, N.V. Karthik, H. Gong, T.L. Starr, B.E. Stucker, Microstructures and mechanical properties of Ti6Al4V parts fabricated by selective laser melting and electron beam melting, J. Mater. Eng. Perform. 22 (2013) 3872–3883, https://doi.org/10.1007/s11665-013-0658-0.
[12] C. Dharmendra, A. Hadadzadeh, B.S. Amirkhiz, A. Lloyd, M. Mohammadi, Deformation mechanisms and fracture of electron beam melted Ti–6Al–4V, Mater. Sci. Eng. 771 (2020) 138652, https://doi.org/10.1016/j.msea.2019.138652.
[13] T. DebRoy, H.L. Wei, J.S. Zuback, T. Mukherjee, J.W. Elmer, J.O. Milewski, A. M. Beese, A. Wilson-Heid, A. De, W. Zhang, Additive manufacturing of metallic components – process, structure and properties, Prog. Mater. Sci. 92 (2018) 112–224, https://doi.org/10.1016/j.pmatsci.2017.10.001.
[14] S. Liu, Y.C. Shin, Additive manufacturing of Ti6Al4V alloy: a review, Mater. Des. 164 (2019) 107552, https://doi.org/10.1016/j.matdes.2018.107552.
[15] J. Ma, J. Tian, M. Yan, Z. Chen, J. Shen, J. Wu, Defect analysis and 2D/3D-EBSD investigation of an electron beam melted Ti-6Al-4V alloy, Mater. Char. 166 (2020) 110440, https://doi.org/10.1016/j.matchar.2020.110440.
[16] M. Simonelli, Y.Y. Tse, C. Tuck, Effect of the build orientation on the mechanical properties and fracture modes of SLM Ti-6Al-4V, Mater. Sci. Eng. 616 (2014) 1–11, https://doi.org/10.1016/j.msea.2014.07.086.

[17] J.S. Keist, T.A. Palmer, Development of strength-hardness relationships in additively manufactured titanium alloys, Mater. Sci. Eng. 693 (2017) 214–224, https://doi.org/10.1016/j.msea.2017.03.102.
[18] S.L. Semiatin, T.R. Bieler, The effect of alpha platelet thickness on plastic flow during hot working of Ti-6Al-4V with a transformed microstructure, Acta Mater. 49 (2001) 3565–3573, https://doi.org/10.1016/S1359-6454(01)00236-1.
[19] W.D. Nix, J.R. Greer, G. Feng, E.T. Lilleodden, Deformation at the nanometer and micrometer length scales: effects of strain gradients and dislocation starvation, Thin Solid Films 515 (2007) 3152–3157, https://doi.org/10.1016/j.tsf.2006.01.030.
[20] M. Haghshenas, Multi-cycling instrumented nanoindentation of a Ti-23Nb-0.7Ta-2Zr-1.2O alloy in annealed condition, Mater. Sci. Eng. 697 (2017) 8–16, https://doi.org/10.1016/j.msea.2017.05.004.
[21] J.R. Greer, W.C. Oliver, W.D. Nix, Size dependence of mechanical properties of gold at the micron scale in the absence of strain gradients, Acta Mater. 53 (2005) 1821–1830, https://doi.org/10.1016/j.actamat.2004.12.031.
[22] K. Durst, B. Backes, O. Franke, M. Göken, Indentation size effect in metallic materials: modeling strength from pop-in to macroscopic hardness using geometrically necessary dislocations, Acta Mater. 54 (2006) 2547–2555, https://doi.org/10.1016/j.actamat.2006.01.036.
[23] H. Gao, Y. Huang, Geometrically necessary dislocation and size-dependent plasticity, Scripta Mater. 48 (2003) 113–118, https://doi.org/10.1016/S1359-6462(02)00329-9.
[24] D.R.C.Q. Ma, Size dependent hardness of silver single crystals Size dependent hardness of silver single crystals, J. Mater. Res. 10 (2015) 853–863.
[25] B.B. Jung, H.K. Lee, H.C. Park, Effect of grain size on the indentation hardness for polycrystalline materials by the modified strain gradient theory, Int. J. Solid Struct. 50 (2013) 2719–2724, https://doi.org/10.1016/j.ijsolstr.2013.05.002.
[26] Z. Zheng, S. Waheed, D.S. Balint, F.P.E. Dunne, Slip transfer across phase boundaries in dual phase titanium alloys and the effect on strain rate sensitivity, Int. J. Plast. 104 (2018) 23–38, https://doi.org/10.1016/j.ijplas.2018.01.011.
[27] T.S. Jun, D.E.J. Armstrong, T.B. Britton, A nanoindentation investigation of local strain rate sensitivity in dual-phase Ti alloys, J. Alloys Compd. 672 (2016) 282–291, https://doi.org/10.1016/j.jallcom.2016.02.146.
[28] T.S. Jun, Z. Zhang, G. Sernicola, F.P.E. Dunne, T.B. Britton, Local strain rate sensitivity of single α phase within a dual-phase Ti alloy, Acta Mater. 107 (2016) 298–309, https://doi.org/10.1016/j.actamat.2016.01.057.
[29] Q. Wei, S. Cheng, K.T. Ramesh, E. Ma, Effect of nanocrystalline and ultrafine grain sizes on the strain rate sensitivity and activation volume: fcc versus bcc metals, Mater. Sci. Eng. 381 (2004) 71–79, https://doi.org/10.1016/j.msea.2004.03.064.
[30] H. Fan, Q. Wang, J.A. El-Awady, D. Raabe, M. Zaiser, Strain rate dependency of dislocation plasticity, Nat. Commun. 12 (2021) 1–11, https://doi.org/10.1038/s41467-021-21939-1.
[31] Q. Wei, Strain rate effects in the ultrafine grain and nanocrystalline regimes-influence on some constitutive responses, J. Mater. Sci. 42 (2007) 1709–1727, https://doi.org/10.1007/s10853-006-0700-9.
[32] A. Pineau, A. Amine Benzerga, T. Pardoen, Failure of metals III: fracture and fatigue of nanostructured metallic materials, Acta Mater. 107 (2016) 508–544, https://doi.org/10.1016/j.actamat.2015.07.049.
[33] R. Laptev, N. Pushilina, E. Kashkarov, M. Syrtanov, E. Stepanova, A. Koptyug, A. Lider, Influence of beam current on microstructure of electron beam melted Ti-6Al-4V alloy, Prog. Nat. Sci. Mater. Int. 29 (2019) 440–446, https://doi.org/10.1016/j.pnsc.2019.04.011.
[34] J. Karimi, C. Suryanarayana, I. Okulov, K.G. Prashanth, Selective laser melting of Ti6Al4V: effect of laser re-melting, Mater. Sci. Eng. 805 (2021) 140558, https://doi.org/10.1016/j.msea.2020.140558.